Renewable Energy 241 (2025) 122135

Contents lists available at ScienceDirect

Renewable Energy

journal homepage: www.elsevier.com/locate/renene

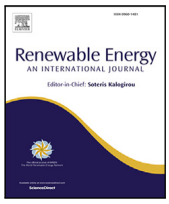

Wind-induced torsion of parabolic trough collectors in operation

Brooke J. Stanislawski *, Ulrike Egerer, Scott Dana, Shashank Yellapantula

National Renewable Energy Laboratory, 15013 Denver W Pkwy, Golden, CO, 80401, USA

ARTICLE INFO

Dataset link: Wind and Structural Loads on Parabolic Trough Solar Collectors at Nevada Solar One (Reference data)

Keywords:
Solar energy
Concentrating solar power
Parabolic trough collectors
Wind loading
Torsion
Field measurements

ABSTRACT

Parabolic trough collector (PTC) systems, a type of concentrating solar power (CSP), use parabolic mirrors to reflect the sun's rays toward an absorber tube to heat the fluid inside. PTCs track the sun throughout the day and are sensitive to angular misalignment, which reduces optical performance. Torsion of the PTC, exacerbated by wind loading, contributes to angular misalignment, which has been quantified by previous studies using numerical simulations and experimental tests. However, angular misalignment due to torsion and wind loading has not yet been studied in an operational plant, which can experience more extreme and variable conditions. This study characterizes the angular misalignment due to torsion at three rows of the Nevada Solar One CSP plant and investigates the influence of wind loading. These findings reveal substantial torsion along the PTC support structure that depends on wind conditions and orientation. Strong winds perpendicular to the PTCs increase the median angular displacement of the outermost row by up to 18 mrad and increase the standard deviation by up to 8 mrad when compared to weak wind conditions. These findings can inform enhanced PTC design, controls and modeling that will improve the performance, reliability and bankability of future CSP plants.

1. Introduction

Concentrating solar power (CSP) provides firm and dispatchable electricity due to its thermal storage and hybridization capabilities. Its inherent capacity to store heat energy for later conversion to electricity makes this technology an integral part of our decarbonized energy future. In China alone, there are 30 ongoing CSP projects expected to produce almost 3000 MW of energy generation capacity in the next 5 years [1]. In the United States, CSP is projected to generate 10% of the nation's electricity by 2050 [2]. CSP technologies include parabolic trough collector (PTC), linear Fresnel, central power tower and parabolic dish systems. Of the 1.7 GW of operational CSP capacity in the United States, PTC systems constitute 73% [2] and are commonly co-located with other CSP or solar photovoltaic technologies to provide available and reliable power production [3].

PTC systems use parabolic mirrors to direct the sun's rays toward the centerline of the absorber tube, which is mounted on every trough along the line of focal points. To track the sun throughout the day, most PTC systems use single-axis, open-loop tracking, typically rotating from facing east at sunrise to facing west at sunset [4]. However, PTC systems can experience misalignment that causes mirrors to point away from the sun, resulting in some or all of the sun's rays missing the absorber tube and reducing optical performance. As angular misalignment increases, more of the sun's rays incident on the PTC miss the absorber tube, as shown in Fig. 1. This behavior is represented by the intercept factor (γ), which is the ratio of the number of sun rays that hit the absorber tube to the number of sun rays that hit the PTC.

Misalignment issues have plagued PTC plants throughout their operational history. Sargent & Lundy LLC Consulting Group [6] reported that, in 1999, the 30-MWe Solar Energy Generating Systems (SEGS) VI CSP plant experienced a 0.6% efficiency loss due to tracking error and structural twist of the LS-2 PTCs and a 2% efficiency loss due to geometric inaccuracies. A numerical study found that a tracking error of 16 mrad resulted in a 60% reduction in optical efficiency [7]. The larger 80-MWe SEGS plant experienced alignment problems and never reached the performance achieved by the SEGS VI plant. Misalignment may be caused by structural deformation, installation position errors, wind loading, gravity, heating, tracking control algorithm, hardware failures and fatigue [3–5,8–11]. The support structure, which comprises the columns and piles, space frame and receiver brackets, is designed to provide the PTC components with stability and rigidity. The space frame transmits the torque of the tracking system and provides rigidity to the mirrors to maintain the designed parabolic shape [9]. Wind-induced structural twist, or torsion, may deform the parabolic shape, thereby strongly reducing the optical performance of PTCs as the heat flux from the collector is not fully captured by the absorber tube [3, 12]. Torsional misalignment can be mitigated through shorter trough segments or increased structural stiffness of the segments [13,14].

* Corresponding author.
E-mail address: brooke.stanislawski@nrel.gov (B.J. Stanislawski).

https://doi.org/10.1016/j.renene.2024.122135
Received 25 April 2024; Received in revised form 11 November 2024; Accepted 8 December 2024
Available online 20 December 2024

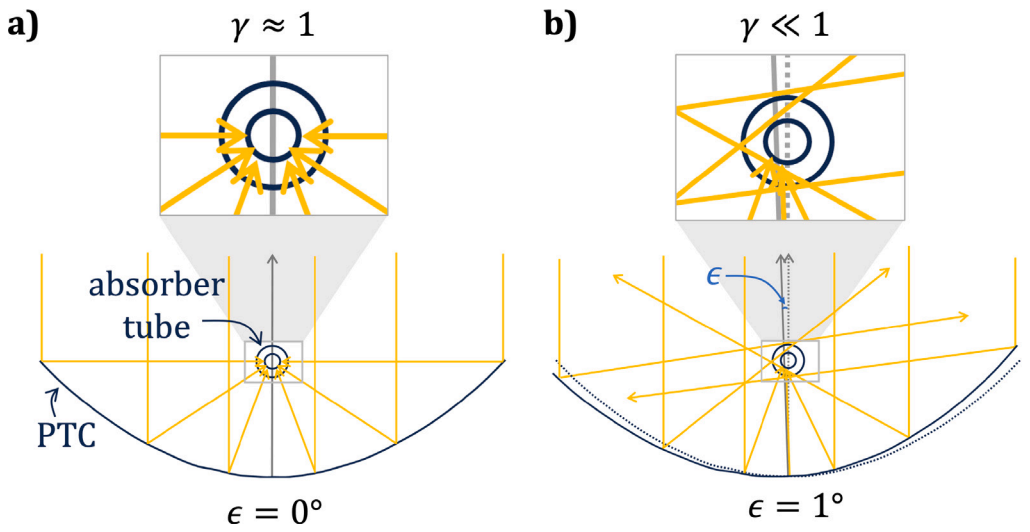

Fig. 1. Diagram of the impact of angular misalignment (ϵ) on the path of the sun rays in the case of (a) no misalignment and (b) 1° of misalignment. Upper images are close-ups. *Source:* Figure adapted from Stanek et al. [5].

Many studies of wind-induced torsion have relied on test bench experiments or numerical simulations. Based on numerical structural analysis, the wind-induced structural twist along the 100-m length of the LS-3 and EuroTrough collectors reaches 8 mrad at a wind speed of 11 m/s, resulting in 55% of the heat flux missing the absorber tube [15,16]. Further, numerical simulations have shown that turbulent wind can cause self-excited torsional vibrations for certain trough angles [17]. Wind-induced forces and displacements of the PTC increase with higher wind speeds, but by varying magnitudes depending on orientation [18,19].

Because the PTCs rotate throughout the day, the influence of orientation (tilt and yaw angle) on the wind-induced misalignment is important. Numerical results from a multiphysics-coupled transient model reveal maximum PTC displacement when the PTC faces away from the wind and minimum displacement when facing down [18]. Based on finite element analysis informed by wind pressure forces from wind tunnel experiments, the mirrors of a PTC experience a maximum peak displacement of 21.7 mm when the PTC is tilted 10 degrees away from the face-up position, toward the wind [20]. This peak displacement is located at the spanwise midpoint between the two support structures of the PTC. Overall, this study emphasizes the strong influence that PTC orientation has on the resulting forces, which is related to the windward exposed area, support structure, flow field and vortex shedding. Thus, understanding torsion along the PTC and how it varies with orientation and wind conditions, especially in an operational setting, is important in mitigating the resulting optical errors and maximizing performance.

The 2020 CSP best practices report [3] highlights the need for low-cost, low-maintenance PTC systems that operate at a high optical and thermal performance and can survive wind and earthquake loads. To this end, extensive research has investigated angular misalignment through numerical and experimental test bench methods; however, there have been no studies of torsion and wind-induced angular misalignment experienced by PTCs in operational settings. Because the operating conditions in the field can be so variable and extreme, differing from wind tunnel flow conditions due to three-dimensional turbulence, terrain and diurnal transitions [21], it is important to study and quantify the wind-driven behavior of PTC systems in operational settings. For example, Egerer et al. [22] observed higher wind-induced static and dynamic loads on support structures in the field than previously reported by wind tunnel tests. The present study aims to characterize the torsion of the PTC support structure observed at three rows in the Nevada Solar One (NSO) CSP plant and assess the influence of wind loading in the torsional misalignment by investigating the following research questions:

1. How does torsional misalignment of PTC support structures vary over time and by location for three rows at an operational CSP plant?
2. How does wind loading affect the torsional misalignment?

Quantification of torsional misalignment and detailed understanding of its causes can lead to targeted mitigation efforts including improved control strategies, system and component design, and performance models that will improve the performance, reliability and bankability of future CSP power plants.

2. Methods

To explore these research questions, the authors analyze PTC tilt angle measurement data from the long-term field measurement campaign at the Nevada Solar One CSP plant [23]. The data are publicly available on the Open Energy Data Initiative [24].

2.1. Field data measurements at Nevada Solar One

The National Renewable Energy Laboratory team conducted a wind and structural loads field measurement campaign at the NSO parabolic trough plant located in Boulder City, Nevada, which has a nominal capacity of 72 MW and 0.5 h of full-load storage. The solar field contains 800 total solar collector assemblies (SCAs), which are grouped into four sub-fields, each containing 50 rows of four 100-m-long SCAs. Each SCA comprises SGNX-1 PTCs, which have an aperture of 5 m and a focal length of 1.49 m, mounted on single-axis trackers.

The PTC tilt angle is determined by a Parker pneumatic hydraulic rotary drive actuator (Parker Special HTR 300) situated on the drive occurrence (DO) pylon. When tracking the sun, the drive tracks in 2.2-mrad (0.125-degree) intervals and the overall rotation is 240° −0°, +2°. The PTC tilt angle is controlled by advanced local controllers in an open-loop controls system that was developed and tested by Solargenix Energy [25]. This controls system measures the angular position of the SCA adjacent to the drive actuator (not on the space frame), but does not measure the actual position of the sun and instead relies on the pre-calculated sun position. Therefore, structural deformation, such as torsion, wind loading, off-design installed PTC or absorber tube position and errors in calculation inputs (e.g., geographic location, elevation) can be detrimental to performance. During high wind speed events, NSO stows the PTCs to prevent damage. For complete details about the field experiment, refer to Egerer et al. [23].

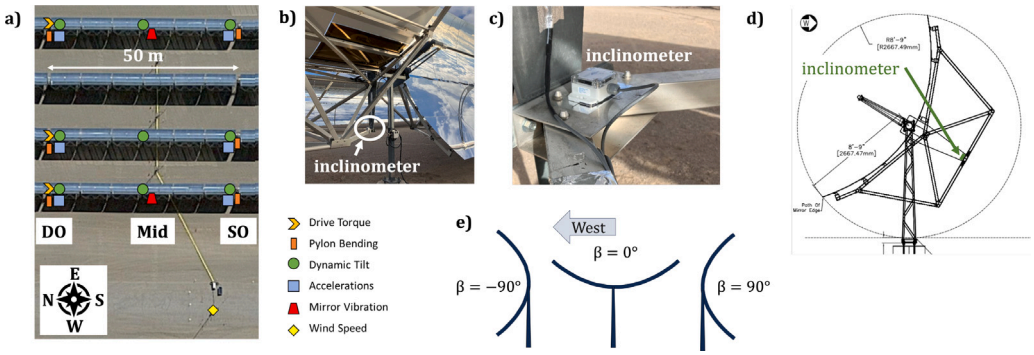

Fig. 2. Instrumentation deployed at the Nevada Solar One CSP plant: (a) overview of the structural loads measurements, (b)–(d) location of the inclinometers used to measure tilt angle and (e) definition of the PTC tilt angle. *Satellite images from ©2023 Google Earth data. Photos by Scott Dana.*

2.1.1. Instrumentation

As part of this campaign, inclinometers were installed to measure the tilt angles of three PTC rows: 1, 2 and 4, counting from the western edge of the solar field. These rows were selected to capture the different flow and loading dynamics at edge rows versus interior rows. As shown in Fig. 2, three inclinometers were installed in each row, spanning half (50 m) of an SCA. The inclinometers measured at a temporal frequency of 20 Hz and with an overall tolerance of ±2.04 mrad (0.1171°). This tolerance includes the manufacturer-provided tolerances of the sensor, manufactured by 2GIG Engineering, and the NI 9239 signal conditioning module manufactured by National Instruments. The combined Category B uncertainty associated with the inclinometer measurement is ±1.75 mrad (0.1005°), which includes both a fixed and percentage reading uncertainty provided by the manufacturers of the inclinometer, data acquisition system and Vishay resistor. Thus, tilt angle measurements are accompanied by a tolerance of ±2.04 mrad.

The PTC tilt angle is controlled by the Parker actuator, which is located in the center of the SCA, at the DO pylon (northern edge of the measurement region). The southern end of the SCA has a loose bearing and is referred to as the shared occurrence (SO) pylon. The inclinometers are mounted on the space frame (Fig. 2) at the DO location, SO location, and centered between the two at the "Mid" location. Data from the inclinometers will be hereon tagged with the row number and location subscripts (e.g., "R1_DO" for measurements from Row 1 at the DO). The mounting surface on the space frame was selected for its ease of installation and reference location definition and because this surface is used by NSO for periodic calibration of the angular position of the PTCs. Because the inclinometers are mounted on the space frame and not on the mirrors, the measurements indicate torsion in the space frame and include any angular offsets among the mounting surfaces of each inclinometer. Nevertheless, any torsion in the space frame is important to quantify because it defines the positions of the mirrors. As an example, Christian and Ho [26] found that rotating the LS-2 PTC from facing up to facing east/west yielded effective slope errors on the order of 1 mrad due to gravity-induced displacements of the PTC support structure and mirrors. However, because the space frame of the LS-2 PTC is different than at NSO, these findings cannot be directly applied to the present case. At NSO, gravity-induced mirror displacements were found to vary by ~1 mrad across all operational tilt angles in rows 1 and 2 [23]. Thus, in addition to any angular offsets among the inclinometer mounting surfaces, angular displacements in the SCAs are expected to affect the positioning of the mirrors with an uncertainty of ~1 mrad.

The inclinometers measure the angle between the inclinometer mounting surface and calibrated earth level [23]. As shown in Fig. 2e, the inclinometers record a zero position when the trough is facing up, a positive angle when facing east and a negative angle when facing west. This instrumentation recorded data from November 2022 through June 2023, but a plant calibration occurred on December 22, 2022, so only data after this date are used in the present analysis. From the field measurement dataset [23,24], this work uses the "raw" tilt angle measurements, not the "calibrated" measurements because the calibration procedure relied on the measured tilt angle when in stow, which was later revealed to not be "locked" position. In this stow position, the PTC tilt angle may vary even though the controls dictate a 120° angular position. The actual angular position of the PTC, as commanded by the control system, was unavailable; therefore, it could not be used for calibration.

To measure inflow wind conditions, a meteorological mast was installed 30 m outside of the PTC array to the west. Sonic anemometers measured wind speed, direction and temperature at heights of 3.5 m, 5 m and 7 m, with a frequency of 20 Hz. A cup anemometer measured the horizontal wind speed at a 15-m height. Temperature, relative humidity and barometric pressure were also measured at a height of 2 m and a frequency of 1 Hz. Analysis of 1-min averaged data was used to characterize torsional error and explore the influence of inflow conditions. The data are filtered to only consider time periods during operation, which excludes stow and includes only daytime periods during which the PTCs are tracking the sun position.

2.2. Calculation of torsional error

Here, torsional error of the SCA is defined as the angular displacement away from a reference angular position along the transversal plane, as shown in Fig. 3. Mathematically, torsional error is defined as the difference between the measured PTC tilt angle at a given location and the measured tilt angle at a reference location:

$$\epsilon_{torsion} = \beta_{x,y} - \beta_{x,DO} \tag{1}$$

where β denotes the measured tilt angle of the PTC at a given location (x, y), where x denotes the row number (R1, R2 or R4) and y denotes the sensor position (DO, Mid or SO) on that row. A torsional error of zero would represent an SCA that exhibits no twisting. The DO location is always used as the reference position because it is the location of the rotational drive and the controller and because of the high stiffness of the SCA assembly at the drive. Because each tilt angle measurement has a tolerance of ±2.04 mrad, the torsional error has an overall tolerance of ±4.08 mrad.

Similar to slope error and tracking error, torsional error describes an angular offset away from the intended aim point of the PTC, and thereby negatively affects optical performance. Torsional error within a row (e.g., $\beta_{R1,SO} - \beta_{R1,DO}$) indicates variation in stiffness along the SCA, which depends on the design and materials used and can be exacerbated by gravity, wind and/or temperature effects. To illuminate how angular misalignment impacts optical performance, Fig. 4 illustrates the intercept factor as a function of angular misalignment for a PTC with the same aperture and focal length as the SGNX-1 and with ideal

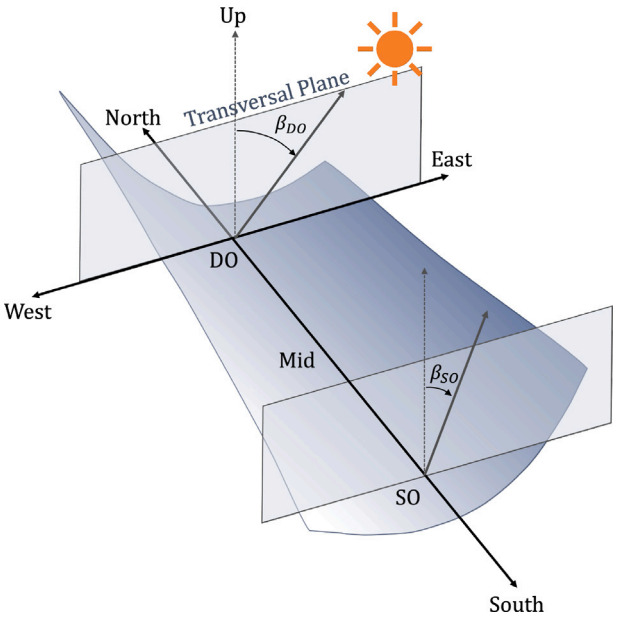

Fig. 3. Angular displacement in the transversal (east–west-up) plane caused by torsion along the PTC. Angular displacement is the difference between the tilt angle, β, measured at the two locations shown, DO and SO. Figure not to scale.

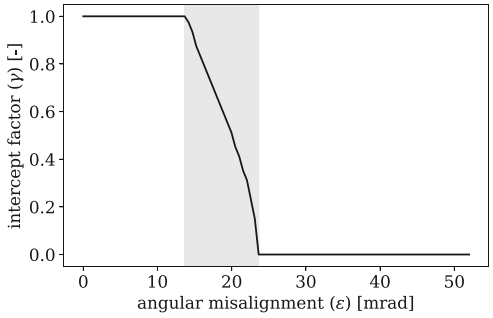

Fig. 4. Intercept factor as a function of angular misalignment ϵ for a PTC with a 5-m aperture and a 1.49-m focal length without sun shape or slope error. The gray region spans the critical angles between 13.7 and 23.6 mrad.

optical properties. These results were generated using FirstOPTIC [27], an analytical solver for the intercept factor, and reveal the dramatic decrease in intercept factor that results from small increases in angular misalignment within the shaded region. This shaded region is bounded by 13.7 mrad (0.78°), the acceptance angle and 23.6 mrad (1.35°). The acceptance angle is the maximum angular misalignment angle at which all rays incident on the PTC hit the absorber tube, resulting in an intercept factor of ~1 without sun shape or slope error. When the angular error is larger than 23.6 mrad, almost none of the rays reflecting off the PTC hits the absorber tube, resulting in an intercept factor of ~0. In between these two angles, the PTC's optical performance depends on the magnitude of the error, as shown in the shaded region of Fig. 4.

3. Results and discussion

3.1. Long-term spatial variations in torsional error

The torsional error is characterized based on measurements at three SCAs during operational, daytime periods of the 7-month measurement period. These results reflect the behavior at three SCAs out of the 800 total SCAs at NSO. Fig. 5 depicts the statistical summary of the torsion experienced by each row during all environmental and operational

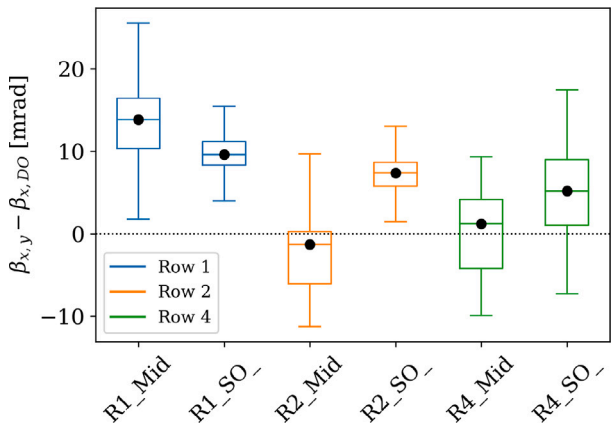

Fig. 5. Statistical summary of the torsional error ($\beta_{x,y} - \beta_{x,DO}$) along each row from December 23, 2022, to June 11, 2023, during daytime hours. The positive torsional error indicates that the PTC at (x, y) is lagging behind the DO position. The negative torsional error indicates that the PTC at (x, y) is ahead of the DO position. The torsional error has a tolerance of ±4.08 mrad.

conditions. Each box plot represents the distribution of the difference between the measured tilt angle at a given location and the measured tilt angle of each row's drive location (e.g., $\beta_{R1,SO} - \beta_{R1,DO}$ for row 1). Positive torsional error, for example in row 1, indicates that the Mid and SO locations in row 1 lag behind the DO location. Existing design practices aim to minimize this lag, which is expected since the SCA is driven and controlled at the DO location, effectively "pulling" the 50-m SCA segments along through the rotation while the SO location is held loosely and the Mid location is free. The magnitude of the torsional error indicates the lack of stiffness in the SCA structure, but also includes any angular offsets among the mounting surfaces of the inclinometers. The negative torsional error in row 2 indicates that the Mid location of the PTC at (x, y) is ahead of the DO position, which is not the expected behavior and may indicate an angular offset between the mounting surfaces.

Within each row, substantial torsional effects are observed. Overall, row 1 experiences the greatest amount of torsion, likely due to the impact of wind loading as an exterior row, whereas row 4 experiences the greatest variability in the torsion. The SCA in row 1 exhibits a median of 13.9 mrad angular displacement at the Mid location and 9.6 mrad angular displacement at the SO location with respect to the DO location. The larger angular displacement at the Mid location reflects a bowing effect as the Mid location lags behind both the outer locations of the PTC, which may be attributed to wind loading and the lack of stiffness at the Mid location. This angular displacement at the Mid location exceeds the acceptance angle of 13.7 mrad, meaning that part of this SCA may suffer from reduced optical performance if the inclinometer mounting surfaces are perfectly aligned. In rows 2 and 4, the SO locations show the largest median deviation at 7.4 mrad and 5.2 mrad, respectively, which may be attributed to their long distance from the drive. In rows 1 and 2, the Mid location has a higher standard deviation (larger box) than the SO location, demonstrating the free movement at this location. The reported torsional error has a tolerance of ±4.08 mrad.

The torsion experienced by these SCAs is likely to negatively impact optical performance and heat flux distribution along the absorber tubes. This problem could be mitigated by increasing the stiffness of the space frame along the length of the SCA or by improving the controls. Currently, the controls determine the PTC tilt angle based on one inclinometer per SCA at the drive location. Adding inclinometers at the mid and shared locations and calculating an "average" optimal tilt angle for the entire PTC might improve optical performance. In closed-loop tracking, adding additional light sensors or inclinometers along the length of the PTC could provide more complete feedback to the controls to correct the PTC tilt angle.

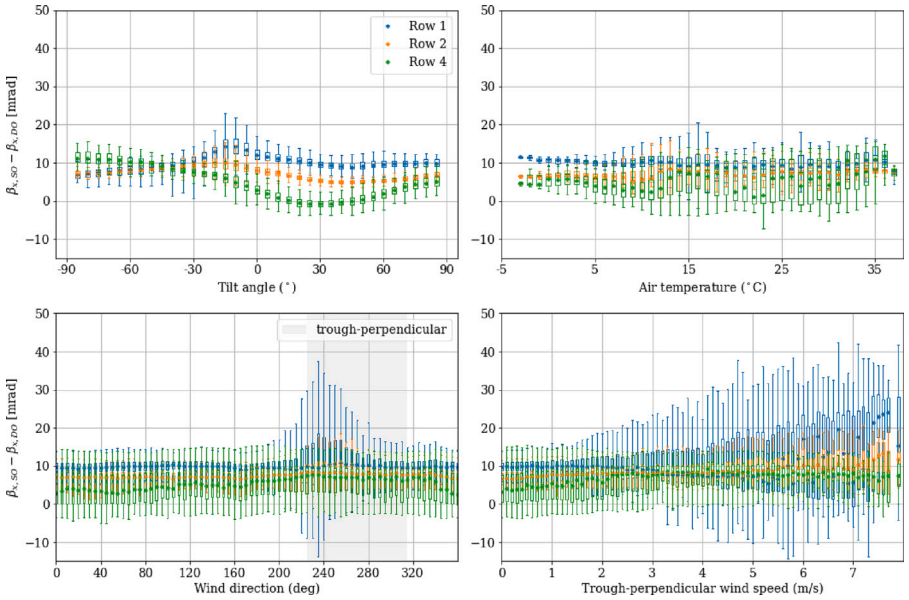

Fig. 6. The relationship between the torsional error at the shared location (SO) of all rows and measured variables, represented using box plots of all daytime, operational data from December 23, 2022, to June 11, 2023. Box plots are shown only when the number of data points exceeds 20. Measured variables include the tilt angle of the PTC, air temperature measured at a 7-m height, inflow wind direction measured at a 7-m height, and the trough-perpendicular component of the inflow wind speed.

3.2. Possible root causes for torsional error variations

The torsional error includes all possible error sources, including gravity, non-uniform distribution of mass, drive accuracy and backlash, structural deformation, assembly stiffness, bearing friction, wind loading, temperature, off-design trough positions and rotation axis position. Fig. 6 illustrates the correlation between torsional error at the SO location of each row and four other measured variables: PTC tilt angle, wind direction, trough-perpendicular wind speed and air temperature. The median torsional error strongly correlates with tilt angle, changing by about 8 mrad in row 1, 5 mrad in row 2 and 11 mrad in row 4 across the range of tilt angles. Rows 1 and 2 show peaks at tilt angles of −10 to −15 degrees, meaning that the SCA is most twisted just after the SCA passes the face-up position, which occurs roughly at solar noon. Although row 2 exhibits symmetric behavior about the peak, row 1 exhibits greater torsional error at positive tilt angles than row 2, perhaps due to wind loading. Gravity effects are expected to apply similarly to all rows, but row 4 reveals a different behavior. This sinusoidal behavior perhaps indicates variations in the sensor positioning on the space frame compared to the other rows or in the mass distribution about the rotation axis. This sinusoidal trend also appears in the hinge moments calculated at the drive shaft [22], which supports the latter explanation. Regarding the influence of temperature, the torsional error in all rows remains largely insensitive, indicating that the thermal expansion of the space frame materials has a small impact relative to PTC orientation and wind conditions.

The lower row of Fig. 6 illustrates the correlation between the torsional error and wind conditions. In these box plots, the median values represent the static wind loading effects and the size of each box — a measure of the standard deviation of the data — represents the dynamic wind loading effects. The median value of all rows remains largely insensitive to the wind direction; however, there is a substantial increase in the standard deviation of the row 1 torsional error, represented implicitly by the upper and lower bounds of the box plots, during southwesterly (225–270 degrees) winds. Row 1 is the most vulnerable to the wind direction as an exterior row and therefore the most sensitive to trough-perpendicular winds from the west. The last subfigure exhibits the correlation between the torsional error and trough-perpendicular wind speed. As expected, row 1 reveals the strongest correlation with wind speed, as illustrated by greater standard deviation and variability in the median as wind speed increases. At high wind speeds (>5 m/s), the median torsional error becomes erratic with a large standard deviation, likely due to the difference in aerodynamic forces pushing against the PTC when turned away versus toward the strong winds.

3.3. Impact of wind conditions on torsional error

The previous section highlighted the sensitivity of torsional error to the wind conditions, which is tested in this section by filtering the data for specific wind conditions to parse out the factors of wind speed, wind direction and tilt angle. Fig. 7 illustrates how torsional error varies with tilt angle during strong, westerly winds (opaque) versus during weak winds from any direction (translucent). Here, the term “strong winds” refers to wind speeds greater than 4 m/s, “weak winds” refers to wind speeds less than 3 m/s, and “westerly” refers to wind directions between 225 and 315 degrees clockwise from north, which are perpendicular to the PTCs. The translucent markers illustrate the baseline angular misalignment without wind effects. Rows 1 and 2 experience a baseline torsional error of approximately 10 mrad due to gravity, distance of SO from the drive, and variation in assembly or component (e.g., bearings) stiffness at the measurement locations. The absolute difference between the opaque and translucent markers represents the wind effects and eliminates the uncertainty associated with possible misalignment of the inclinometer mounting surfaces. The wind effects are the most noticeable in row 1 and diminish as one moves farther into the interior of the collector field. In all rows, the wind conditions impact the torsional error at angles between −20 and +40 degrees, with maximum differences at 0 degrees in rows 2 and 4, which aligns with Mehos et al. [3], who stated that “the face-up orientation is typically the most exposed and dangerous”. At zero or positive tilt angles, strong westerly winds change the median torsional error by up to 18 mrad in row 1, 8 mrad in row 2 and 6 mrad in row 4. At negative tilt angles less than −15 degrees, strong westerly winds change the median torsional error by up to 9 mrad in row 1, but do not affect the torsional error in rows 2 and 4. Compared to the weak wind condition results, which depict symmetric behavior about the peak in row 1, the strong westerly winds induce a dramatic asymmetry about this tilt angle of −15 degrees because of the parabolic shape. This critical tilt angle of −15 degrees aligns with the finite element

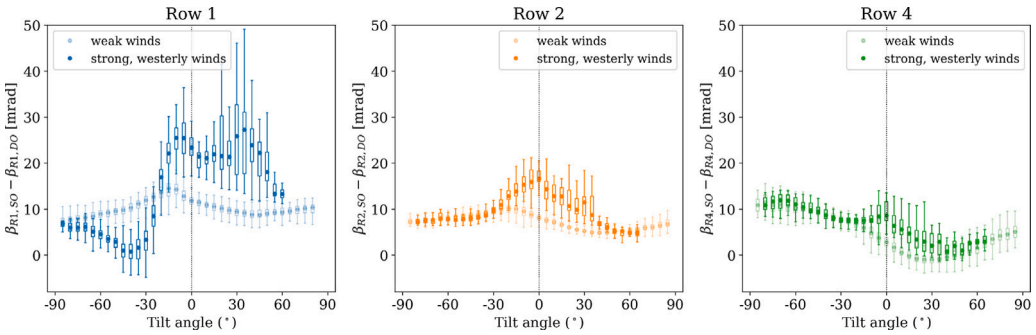

Fig. 7. The relationship between torsional error at the shared location (SO) and tilt angle for strong wind conditions (opaque markers) versus weak wind conditions (translucent markers). Results are represented using box plots of all daytime, operational data from December 23, 2022, to June 11, 2023. Box plots shown only when the number of data points exceeds 20.

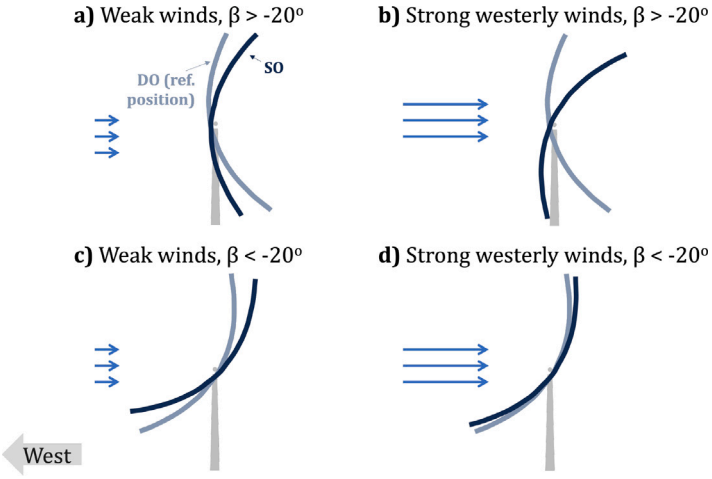

Fig. 8. The angular displacement induced by weak winds versus strong westerly winds when the PTC faces away from the wind ($\beta > -20°$) versus toward the wind ($\beta < -20°$). Angular misalignment is exaggerated for clarity.

analysis results from Zou et al. [20], who identified a maximum peak displacement of the mirrors when the PTC is tilted 10 degrees toward the wind from face-up.

These findings reveal a clear dependence of the torsional error on both tilt angle and wind conditions. During strong westerly winds, row 1 experiences a trend similar to that in rows 2 and 4 at positive angles, but deviates dramatically at angles less than (more west-facing) than −15 degrees, which exemplifies the influence of the wind-induced deflection as the PTC exposes more interior surface area to the wind. This interaction between PTC orientation and the inflow wind is depicted in Fig. 8. During weak winds, the SO location of row 1 lags behind the DO location by between 9 and 14 mrad (Fig. 8**a,c**). During strong, westerly winds, row 1 at SO lags behind DO even more, by up to 27 mrad when facing eastward ($\beta > 0$). The peak row 1 torsional error at the 35-degree tilt angle coincides with the peak hinge moment [22], which indicates stronger aerodynamic forces acting on the upper part of the outer surface of the PTC at this position unlike when the PTC faces directly east ($\beta = 90$ deg) and the forces acting on the upper part of the PTC are counteracted by those acting on the lower part. At tilt angles less than −15 degrees, the strong winds cause torsional error to drop to almost zero, indicating minimal twist in row 1. As depicted in Fig. 8**b,d**, when the wind impinges on the outside, convex surface of the PTC, the aerodynamic force rotates the PTC to face more eastward. However, when the wind impinges on the inside, concave surface of the PTC, the same aerodynamic force results in rotating the PTC to face more westward. This stark difference between the strong and weak wind conditions at negative tilt angles does not appear in rows 2 or 4 because row 1 blocks the incoming wind.

To test the hypothesis that torsional error differs based on the eastward versus westward orientation of the PTC, Fig. 6 is recreated for row 1, but using filtered data that distinguishes between times when the PTC faces eastward (facing away from the wind) versus westward (facing toward the wind). As shown in Fig. 8, wind speed has the opposite effect on torsional error depending on PTC orientation when the row 1 PTC faces eastward versus westward. When the PTC faces east, which is pointed away from the incoming trough-perpendicular wind, the torsional error increases as wind speed increases because the aerodynamic forces rotate the PTC downward at the looser SO and Mid locations, increasing the lag between DO and SO. In contrast, when the PTC faces west, which is pointed toward the incoming wind, the torsional error decreases as wind speed increases, because the aerodynamic forces act on the inside of the PTC and push it downward, resulting in more downward rotation at the SO and Mid locations. Because the PTC is facing the wind, this downward rotation reduces the lag between DO and SO, as depicted in Fig. 8. Flow simulations from previous studies [19,28] illustrate the wind flow patterns that affect the PTC support structure stability and tracking system due to stronger eddies on the leeward side of the PTC when it faces the wind versus away from the wind. The wind's impact on torsion is stronger when the PTCs face away from the wind than when they face toward the wind, as highlighted by the steeper slope of the east-facing curve in Fig. 9.

The median torsional error explored in previous sections illustrates the impact of static wind loading, whereas the standard deviation reveals the impact of dynamic wind loading. Fig. 10 quantifies the variability in the torsional error over the entire measurement period during strong, westerly winds (opaque lines), as compared to weak winds (translucent lines). During strong westerly winds, the standard

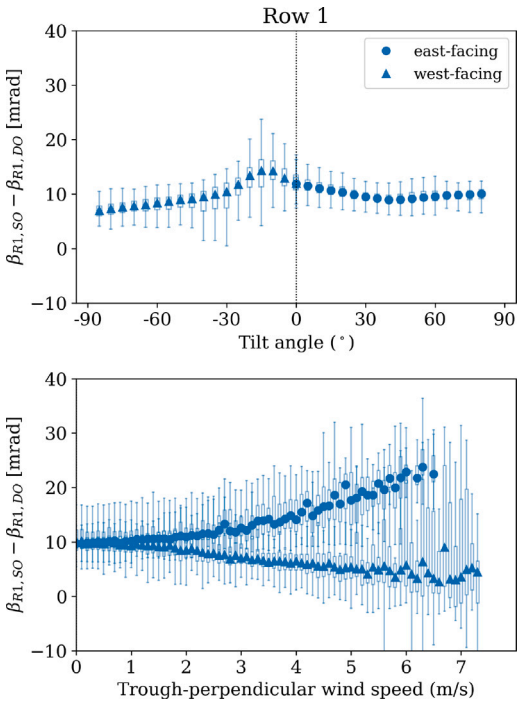

Fig. 9. The relationship between the torsional error at the shared location (SO) of row 1 and the tilt angle and trough-perpendicular wind speed for the east-facing (circle markers) versus west-facing (triangle markers) PTC. Results are represented using box plots of all daytime, operational data from December 23, 2022, to June 11, 2023. Box plots are shown only when the number of data points exceeds 20.

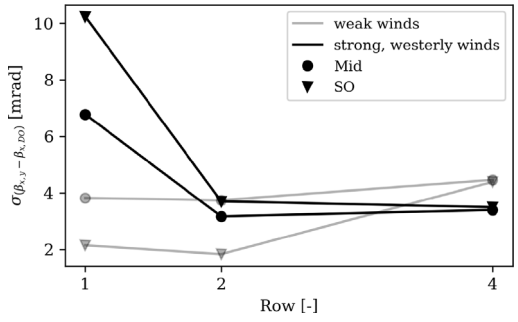

Fig. 10. Standard deviation of torsional error ($\beta_{x,y} - \beta_{x,SO}$) at each row from December 23, 2022, to June 11, 2023, during strong westerly winds (opaque lines), as compared to weak winds (translucent lines).

deviation of torsional error is greatest in row 1, substantially greater than in weak wind conditions, and decreases dramatically in row 2 because row 1 provides sheltering to interior rows. Although the standard deviation of torsional error in row 1 reaches only 3.8 mrad during low wind speeds, the wind-induced variability in torsion leads to an increase in standard deviation up to 10.2 mrad. This increase is because the row 1 PTC faces the undisturbed, turbulent inflow wind and deforms due to the variable, dynamic wind loading. The high standard deviation at row 1 during windy conditions approaches the acceptance angle of the PTC, potentially reducing optical performance. These findings have the potential to improve SCA designs that mitigate dynamic wind effects on optical performance.

To differentiate between the sensitivity of the torsional error to the wind direction versus to the tilt angle, see Fig. 11. The greatest torsional error (in red) occurs at row 1 during strong southwesterly winds at tilt angles between −20 and 50 degrees because the wind loading is more influential when the PTCs face away from the wind. The peak torsional error in red aligns with the greatest hinge moments (C_{my}) of the drive shaft [22]. During all other wind directions, the change in torsional error is much less sensitive to orientation because the wind is blowing along the PTC (not perpendicular to the PTC), without much blockage or flow modification by the PTCs. Row 2 follows a similar trend to that of row 1, but with a smaller magnitude, due to the sheltering effect of row 1 from the wind. During strong westerly winds, the torsional error in the first two rows is more sensitive to the wind direction than to the tilt angle. The row 4 torsional error exhibits the sinusoidal behavior shown in Fig. 6 and in the hinge moments [22]. There is a slight sensitivity to wind direction when facing up during westerly winds, but the row 4 torsional error is more sensitive to tilt angle and largely insensitive to wind direction.

3.4. Torsional error time series during 3 sample days

To provide an idea of how these findings affect daily operations, Fig. 12 illustrates the temporal and spatial variations in torsional error on 3 days: January 28, 2023, which is characterized by low wind speeds and largely uninterrupted operation, February 22, 2023, which is characterized by strong westerly winds and April 2, 2023, which sees a frontal passage as the wind accelerates and changes direction midday. January 28, 2023, the first column of this figure, reveals the typical behavior of the row 1 SCA throughout the day without the influence of wind. The torsional error at the Mid and SO locations is approximately 10 mrad until midday, when the torsional error peaks and then decreases in the afternoon. This trend mirrors that of the median values in Fig. 6, illustrating the influence of SCA tilt angle in torsion. The persistent lag of the SCA at the Mid and SO locations of approximately 10 mrad may also contribute to the peaks occurring slightly after solar noon. As DO rotates to the face-up position, SO is approximately 10 mrad behind. When DO passes the face-up position, gravity begins to pull the DO and SO ends of the SCA in opposite directions. In the last row, the standard deviation of the tilt angle remains approximately 0.1 mrad.

On February 22, 2023, when the plant is operating, the sustained strong westerly winds cause the torsional error in row 1 to quadruple at the SO location until about 13:00 h when the PTC rotates to face the wind, causing the aerodynamic forces to rotate the PTC downward and reducing the torsional lag. Additionally, the torsional error exhibits a large amount of scatter, indicating dynamic wind-loading effects as the turbulence levels increase with the greater wind speeds. This dynamic loading is also illustrated by the standard deviation of tilt angle on this day, which reaches up to 3x its value during weak winds on January 28, 2023.

April 2, 2023 exhibits a real-time transition from the weak winds condition to the strong westerly winds condition. The torsional error increases sharply at 13:00 h when the front passes through the plant. This peak is followed by a sharp drop in torsional error as the PTC rotates to face the wind and the Mid and SO locations are pushed downward by the resulting aerodynamic forces, reducing the lag between those locations and DO. From these three sample days, it is clear that the wind conditions play an important role in torsion, and that the wind's impact depends on the orientation of the PTCs.

4. Conclusion

This study characterizes the torsional error in the PTC support structure experienced by three rows at an operational CSP plant and quantifies the wind impacts on torsion. Wind-induced torsion had been studied using numerical simulations and experimental tests, but not in an operational setting, highlighting a novel contribution of the present study. The findings of this work are summarized in the following conclusions:

- Torsion along the PTC support structure causes a median angular displacement of up to 13.9 mrad in row 1, 7.4 mrad in row 2 and 5.2 mrad in row 4, each with a tolerance of ±4.08 mrad.

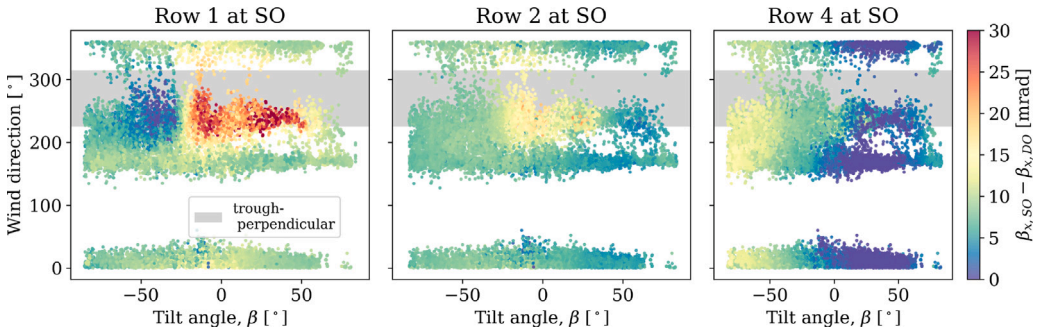

Fig. 11. Torsional error ($\beta_{x,SO} - \beta_{x,DO}$) as a function of tilt angle and wind direction. The gray region signifies westerly winds that are perpendicular to the trough. Data points are from all daytime operational periods during strong winds (>4 m/s) between December 23, 2022, and June 11, 2023.

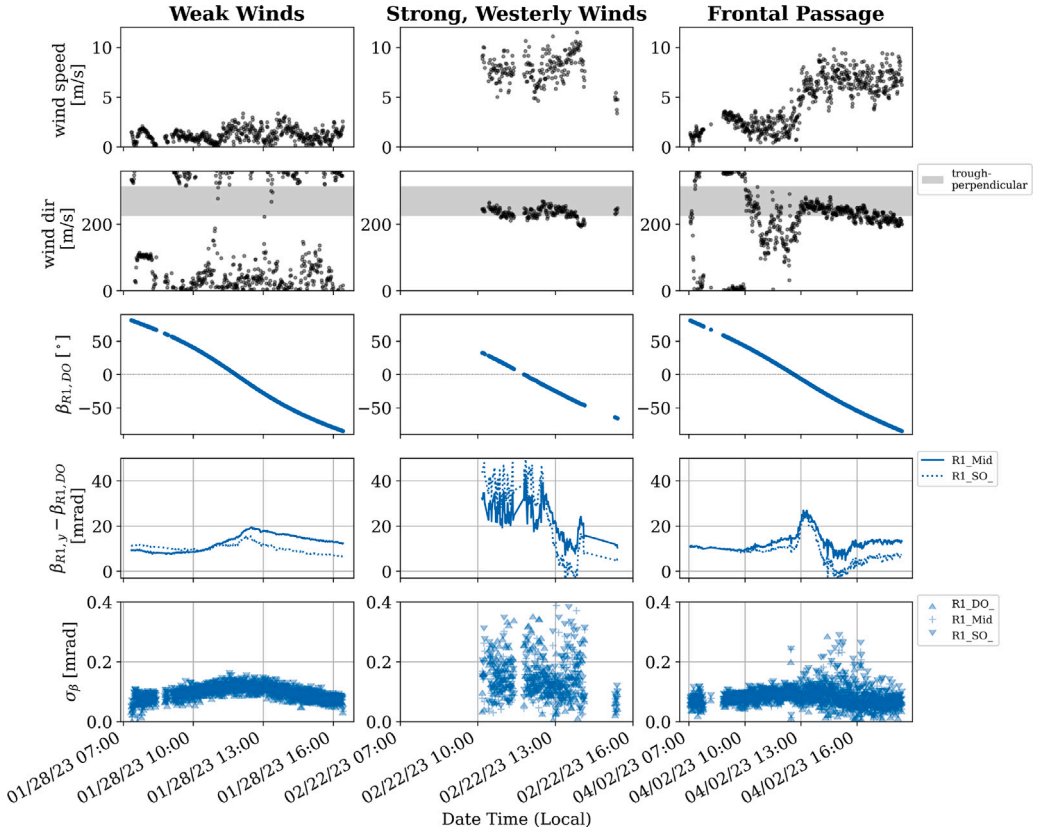

Fig. 12. Measurement data from 3 days: January 28, 2023 (low wind, smooth operation), February 22, 2023 (high winds) and April 2, 2023 (frontal passage). First row: inflow wind speeds at a 7-m height. Second row: wind direction with westerly winds shaded in gray. Third row: PTC tilt angle at row 1, DO $\beta_{R1,DO}$ in degrees. Fourth row: torsional error in row 1 at two lateral locations (Mid and SO), with respect to the drive location (DO). Positive torsional error ($\epsilon_{torsion} > 0$) indicates when the PTC at (x, y) is lagging behind the DO position. Fifth row: standard deviation of 1-min intervals of the PTC tilt angle.

- The median torsional error changes by about 5 to 11 mrad across the full range of tilt angles during operation, peaking in rows 1 and 2 at −15 to −20 degrees (facing slightly toward the west).
- The torsional error in all rows is strongly correlated with trough tilt angle, and in row 1, with trough-perpendicular wind speed as well. Air temperature does not play an influential role in torsional error.

These conclusions are based on measurements from inclinometers mounted on the space frames, which define the position of the mirrors. Future work should quantify the expected orientation and deformation of the mirrors based on the observed torsion of the space frame. These large magnitudes of torsional error include any possible misalignment of the inclinometer mounting surfaces, but the variation and trends suggest potential impacts on optical performance. These findings are based on only three SCAs out of the 800 total SCAs at NSO; therefore, impacts on the overall plant performance are unknown. Although current design practices aim to minimize torsion along the PTC, the torsion experienced at NSO may reduce optical performance in the three measured rows. These findings should be considered in the design of the support structures and control strategies.

Although CSP plants stow the PTCs during strong winds, operational PTCs can still face adverse wind conditions that may exacerbate torsion enough to reduce optical performance. This study finds that torsional error depends strongly on wind conditions, PTC orientation, and the PTC's location within the collector field. Specifically, this study quantifies the effect of wind conditions on the torsional error, summarized in the following conclusions:

- As expected, strong winds (>4 m/s) perpendicular to the PTCs induce greater median torsional error and standard deviation of

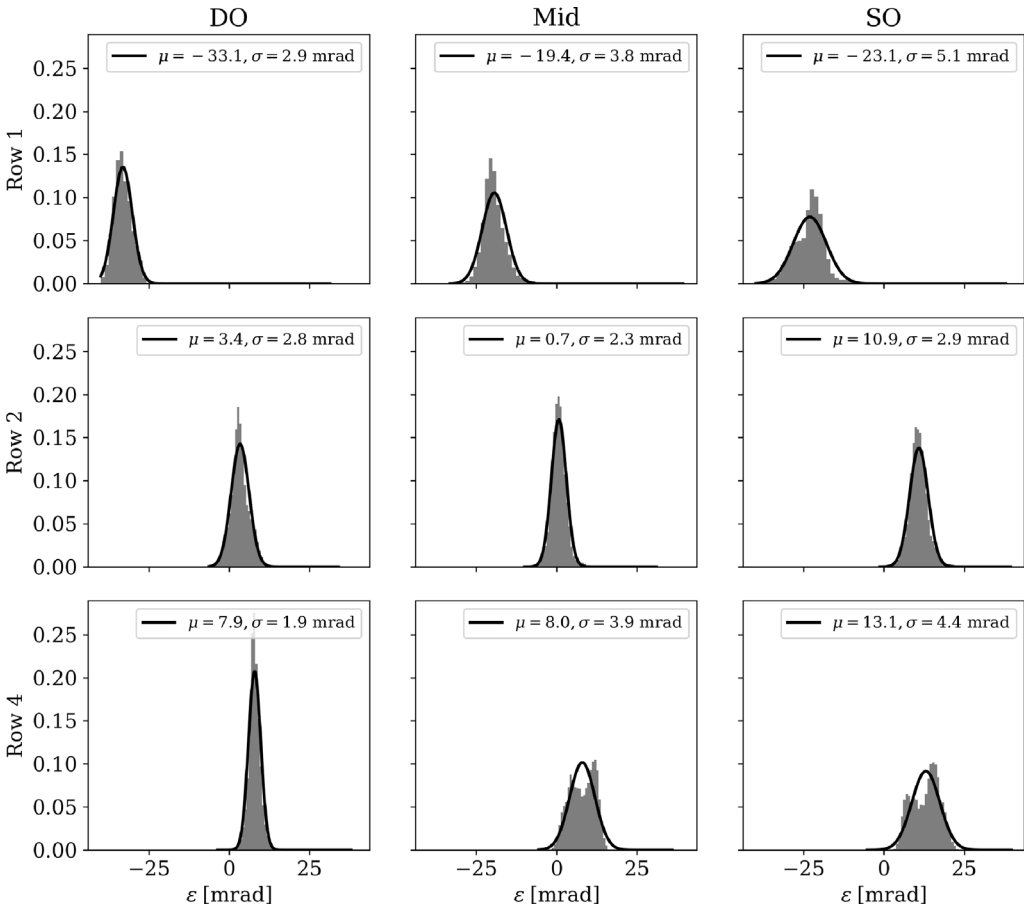

Fig. A.1. Statistical summary of the tracking error ϵ of all operational daytime periods from December 23, 2022, to June 11, 2023.

tilt angle in row 1 than in rows 2 and 4 because row 1 blocks the incoming wind.

- Strong winds perpendicular to the PTCs increase the median torsional error of the outermost row by up to 18 mrad and increase the standard deviation by up to 8 mrad when compared to weak wind conditions.
- Strong winds perpendicular to the PTCs have opposite effects on row 1 torsional error when the troughs face toward versus away from the incoming wind. The parabolic shape causes the transition between reducing and increasing torsional error to occur at a tilt angle of −20 degrees (tilted slightly toward the wind) rather than at 0 degrees (facing up).
- At tilt angles less than −20 degrees (more west-facing), strong winds perpendicular to the PTCs change the median torsional error by up to 9 mrad in row 1 and by a negligible amount in rows 2 and 4.
- At tilt angles greater than −20 degrees (more east-facing), the interior rows 2 and 4 are still affected by strong winds perpendicular to the PTCs, which increase the median torsional error by up to 8.5 mrad in row 2 and 6 mrad in row 4 in the face-up position.
- During strong winds perpendicular to the PTCs, the standard deviation of row 1 torsional error can reach above 10 mrad at the shared location and 6 mrad at the middle of the PTC, compared to weak wind conditions.
- In row 4, an asymmetric distribution of mass about the rotation axis is suspected, which likely causes the sinusoidal behavior of the torsional error time series and the large standard deviation.

Torsional error greater than the acceptance angle of 13.7 mrad will decrease optical performance of the PTC at that location according to the relationship in Fig. 4 and smaller torsional error values can lead to non-uniform heating of the absorber tube. Therefore, the prominent influence of wind in angular misalignment supports the need for stringent torsional stiffness design requirements, torsion mitigation strategies, frequent calibration of the tracker drives and closed-loop control strategies that use a light sensor mounted on the trough to correct misalignment [9].

Based on the data collection and analysis, this work also shares lessons learned from the measurement campaign. The measurement of PTC angular misalignment is difficult in an operational plant that uses open-loop tracking because there is no “ground truth”, and therefore, no way to calibrate the measurements. This means that inclinometer measurements cannot be used for assessing absolute tracking error or optical performance, but rather torsion of the space frame with respect to a reference angular position on the same space frame. This is a helpful lesson to share with the broader CSP community and presents a need for finding a method to establish a “ground truth” at operational PTC plants. To help address these measurement challenges, future work should study the impact of static and dynamic wind loading on optical performance through numerical simulations or in a more controlled experimental test bench setup with heat flux distribution verification capabilities. These findings and lessons learned advance the CSP community’s understanding of torsion and, more broadly, angular displacement error, as well as its measurement, causes and impact, which can inform improved designs, controls and performance modeling techniques. Greater understanding and mitigation of these sources of error promote the continued adoption of CSP and its role in our transition to a clean energy future.

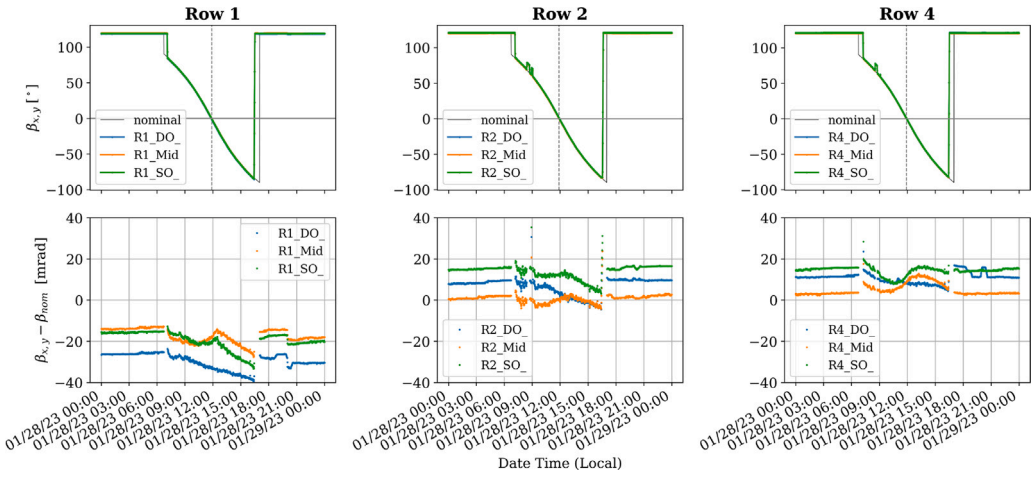

Fig. A.2. Trough tilt angles at rows 1, 2 and 4 and at three lateral locations (DO, Mid, SO) on a low-wind, smooth-operation day (January 28, 2023). Upper row: the trough tilt angle $\beta_{x,y}$ in degrees. Lower row: tracking error ϵ.

CRediT authorship contribution statement

Brooke J. Stanislawski: Writing – review & editing, Writing – original draft, Visualization, Validation, Software, Formal analysis, Data curation, Conceptualization. **Ulrike Egerer:** Writing – review & editing, Visualization, Validation, Data curation. **Scott Dana:** Validation, Methodology, Investigation, Data curation. **Shashank Yellapantula:** Writing – review & editing, Supervision, Resources, Methodology, Funding acquisition, Conceptualization.

Declaration of competing interest

The authors declare that they have no known competing financial interests or personal relationships that could have appeared to influence the work reported in this paper.

Acknowledgments

This work was authored by the National Renewable Energy Laboratory, operated by Alliance for Sustainable Energy, LLC, for the U.S. Department of Energy (DOE) under Contract No. DE-AC36-08GO28308. Funding provided by the U.S. Department of Energy Office of Energy Efficiency and Renewable Energy Solar Energy Technologies Office. The views expressed in the article do not necessarily represent the views of the DOE or the U.S. Government. The U.S. Government retains and the publisher, by accepting the article for publication, acknowledges that the U.S. Government retains a nonexclusive, paid-up, irrevocable, worldwide license to publish or reproduce the published form of this work, or allow others to do so, for U.S. Government purposes. We gratefully acknowledge the guidance of Mark Mehos and Guangdong Zhu from the National Renewable Energy Laboratory, as well as Patrick Marcotte and Hank Price from SolarDynamics, LLC. We are also thankful to Krys Rootham, David Sledge, Henry Sayarath and the entire operations team at Nevada Solar One for their support during and following the measurement campaign.

Appendix. Uncalibrated long-term tracking error

In light of the lack of calibration of the measured PTC tilt angle with the controller-defined tilt angle, results thus far are presented in terms of torsional error, which is the difference between the measured tilt angle at two locations along the same PTC. This section also shares the raw tracking error results—the difference between the measured PTC tilt angle and the calculated sun position. These findings reveal the need for redundant measurements from different metrology techniques when measuring tilt angle (e.g., inclinometer and photogrammetry) and the benefits of saving the controls history at CSP plants.

The tracking error is calculated at every instant in time as:

$$\epsilon = \beta_{x,y} - \beta_{nominal} \tag{A.1}$$

where ϵ denotes the tracking error in milliradians, $\beta_{x,y}$ denotes the measured tilt angle of the PTC at location (x, y) and $\beta_{nominal}$ denotes the nominal tilt angle of the PTC.

The nominal tilt angle, $\beta_{nominal}$, is the tilt angle of the PTC when pointed directly at the calculated sun position in the transversal plane. The sun position is calculated using a `pvlib` [29] Python library for the National Renewable Energy Laboratory's Solar Position Algorithm[1] [30,31], which takes as inputs the latitude, longitude and elevation of NSO and generates the azimuth, γ_{sun}, and elevation, α_{sun}, angles of the sun throughout the field measurement period. These angles are used to project the sun position in 3D onto the east–west-up transversal plane based on Anderson and Mikofski [32] using the `pvlib.tracking` package, which also requires the tilt of the tracker rotation axis with respect to the horizontal ($\beta_a = 0°$) and compass direction along which the axis of rotation lies; measured east of north ($\gamma_a = 0.3°$).

The statistical summary of the raw tracking error from December 23, 2022, to June 11, 2023, is presented in Fig. A.1. The large mean values are likely due to an angular offset between the inclinometer's mounting surface and the aim direction of the mirrors, which could not be quantified due to the lack of calibration. The large standard deviations are likely due to differences in the sun position algorithm used, wind loading (largest at row 1 SO), and asymmetric mass distribution about the pivot axis (at row 4 Mid and SO). This offset between the center of mass and the pivot axis that causes the sinusoidal signal is apparent in the bimodal shape of the histogram at the row 4 Mid and SO locations.

A sample time series tracking error is shown in Fig. A.2 for the low-wind case of January 28, 2023. The second row of figures highlights the trends of tracking error throughout the day. At each sensor location (differentiated by colors), the PTCs move similarly throughout the day, but row 1 appears to track ahead of the sun ($\epsilon < 0$) and rows 2 and 4 appear to lag behind the sun ($\epsilon > 0$). However, in reality, whether the tracking error is positive or negative is unknown due to the lack of calibration. At the drive location in row 1, the tracking error increases approximately linearly throughout the day, up to a tracking

[1] https://pvlib-python.readthedocs.io/en/v0.4.2/generated/pvlib.solarposition.spa_python.html#pvlib.solarposition.spa_python.

error of −40 mrad. In rows 2 and 4, the trend strays from linear and the tracking error appears to decrease in the afternoon in row 2. The tracking error at the Mid and SO locations reveals local error minima just after solar noon (vertical dashed line in the upper row of figures), with the most pronounced peaks in row 1. This tracking error could be due to installation and positioning errors of the SCAs, pivot-point offset of the inclinometer or SCAs, miscalculation of sun position by the controller or deformation of the space frame between the mirrors and inclinometer position.

Data availability

Wind and Structural Loads on Parabolic Trough Solar Collectors at Nevada Solar One (Reference data) (Open Energy Data Initiative (OEDI))

References

[1] CSP project in China, 2022, https://www.solarpaces.org/china-now-has-30-csp-projects-with-thermal-energy-storage-underway/. (Accessed 2 November 2023).

[2] National Renewable Energy Laboratory, The Solar Futures Study, 2021, URL: https://www.osti.gov/biblio/1820105.

[3] M. Mehos, H. Price, R. Cable, D. Kearney, B. Kelly, G. Kolb, F. Morse, Concentrating Solar Power Best Practices Study, Technical Report NREL/TP-5500-75763, National Renewable Energy Laboratory, Golden, CO, 2020, p. 269, URL: https://www.nrel.gov/docs/fy20osti/75763.pdf.

[4] W. Zhang, L. Duan, J. Wang, X. Ba, Z. Zhang, R. Tian, Influences of tracking and installation errors on the optical performance of a parabolic trough collector with heat pipe evacuated tube, Sustain. Energy Technol. Assess. 50 (2022) 101721, http://dx.doi.org/10.1016/j.seta.2021.101721, URL: https://linkinghub.elsevier.com/retrieve/pii/S2213138821007359.

[5] B. Stanek, D. Węcel, Ł. Bartela, S. Rulik, Solar tracker error impact on linear absorbers efficiency in parabolic trough collector – Optical and thermodynamic study, Renew. Energy 196 (2022) 598–609, http://dx.doi.org/10.1016/j.renene.2022.07.021, URL: https://linkinghub.elsevier.com/retrieve/pii/S0960148122010175.

[6] N.G. Sargent & Lundy LLC Consulting Group, Assessment of Parabolic Trough and Power Tower Solar Technology Cost and Performance Forecasts, Technical Report NREL/SR-550-34440, 15005520, 2003, http://dx.doi.org/10.2172/15005520, URL: http://www.osti.gov/servlets/purl/15005520/.

[7] O.B. Belkacem Agagna, A. Smaili, Performance analysis of parabolic trough solar collector under varying optical errors, Energy Sources A 44 (1) (2022) 1189–1207, http://dx.doi.org/10.1080/15567036.2022.2052385, arXiv:https://doi.org/10.1080/15567036.2022.2052385.

[8] G. Zhu, C. Augustine, R. Mitchell, M. Muller, P. Kurup, A. Zolan, S. Yellapantula, R. Brost, K. Armijo, J. Sment, R. Schaller, M. Gordon, M. Collins, J. Coventry, J. Pye, M. Cholette, G. Picotti, M. Arjomandi, M. Emes, D. Potter, M. Rae, Roadmap to Advance Heliostat Technologies for Concentrating Solar-Thermal Power, Technical Report NREL/TP-5700-83041, 2022, http://dx.doi.org/10.2172/1888029, URL: https://www.osti.gov/servlets/purl/1888029/.

[9] P.D. Tagle-Salazar, K.D. Nigam, C.I. Rivera-Solorio, Parabolic trough solar collectors: A general overview of technology, industrial applications, energy market, modeling, and standards, Green Process. Synth. 9 (1) (2020) 595–649, http://dx.doi.org/10.1515/gps-2020-0059, URL: https://www.degruyter.com/document/doi/10.1515/gps-2020-0059/html.

[10] F.M.A. Lorilla, R. Barroca, Challenges and recent developments in solar tracking strategies for concentrated solar parabolic dish, Indones. J. Electr. Eng. Comput. Sci. 26 (3) (2022) 1368, http://dx.doi.org/10.11591/ijeecs.v26.i3.pp1368-1378, URL: http://ijeecs.iaescore.com/index.php/IJEECS/article/view/25062.

[11] B. Yang, S. Liu, R. Zhang, X. Yu, Influence of reflector installation errors on optical-thermal performance of parabolic trough collectors based on a MCRT - FVM coupled model, Renew. Energy 185 (2022) 1006–1017, http://dx.doi.org/10.1016/j.renene.2021.12.102, URL: https://linkinghub.elsevier.com/retrieve/pii/S0960148121018292.

[12] L. Murphy, Wind Loading on Tracking and Field-Mounted Solar Collectors, Technical Report SERI-TP-632-958, 6889663, 1980, http://dx.doi.org/10.2172/6889663, URL: http://www.osti.gov/servlets/purl/6889663/.

[13] G. Weinrebe, Z. Abul-Ella, W. Schiel, On the influence of parabolic trough collector stiffness and length on performance, in: Solar Paces Conference, 2011.

[14] U. Winkelmann, C. Kämper, R. Höffer, P. Forman, M.A. Ahrens, P. Mark, Wind actions on large-aperture parabolic trough solar collectors: Wind tunnel tests and structural analysis, Renew. Energy 146 (2020) 2390–2407, http://dx.doi.org/10.1016/j.renene.2019.08.057.

[15] E. Lüpfert, M. Geyer, W. Schiel, A. Esteban, R. Osuna, E. Zarza, P. Nava, EuroTrough Design Issues and Prototype Testing at PSA, in: International Solar Energy Conference, Solar Engineering 2001: (FORUM 2001: Solar Energy — The Power to Choose), 2001, http://dx.doi.org/10.1115/SED2001-149, _eprint: https://asmedigitalcollection.asme.org/ISEC/proceedings-pdf/SED2001/16702/387/6510407/387_1.pdf.

[16] H. Sun, B. Gong, Q. Yao, A review of wind loads on heliostats and trough collectors, Renew. Sustain. Energy Rev. 32 (2014) 206–221, http://dx.doi.org/10.1016/j.rser.2014.01.032, URL: https://linkinghub.elsevier.com/retrieve/pii/S1364032114000434.

[17] M. Andre, M. Péntek, K.-U. Bletzinger, R. Wüchner, Aeroelastic simulation of the wind-excited torsional vibration of a parabolic trough solar collector, J. Wind Eng. Ind. Aerodyn. 165 (2017) 67–78, http://dx.doi.org/10.1016/j.jweia.2017.03.005.

[18] Z. Zhang, J. Sun, L. Wang, J.J. Wei, Multiphysics-coupled study of wind load effects on optical performance of parabolic trough collector, Sol. Energy 207 (2020) 1078–1087, http://dx.doi.org/10.1016/j.solener.2020.06.107, URL: https://linkinghub.elsevier.com/retrieve/pii/S0038092X20307210.

[19] N. Naeeni, M. Yaghoubi, Analysis of wind flow around a parabolic collector (1) fluid flow, Renew. Energy 32 (11) (2007) 1898–1916, http://dx.doi.org/10.1016/j.renene.2006.10.004, URL: https://linkinghub.elsevier.com/retrieve/pii/S0960148106002734.

[20] Q. Zou, Z. Li, H. Wu, F. Zou, B. Wu, Wind-induced response and pedestal internal force analysis of a Trough Solar Collector, J. Wind Eng. Ind. Aerodyn. 193 (2019) 103950, http://dx.doi.org/10.1016/j.jweia.2019.103950, URL: https://linkinghub.elsevier.com/retrieve/pii/S0167610519305380.

[21] M.J. Emes, M. Marano, M. Arjomandi, Heliostat wind loads in the atmospheric boundary layer (ABL): Reconciling field measurements with wind tunnel experiments, Sol. Energy 277 (2024) 112742, http://dx.doi.org/10.1016/j.solener.2024.112742, URL: https://linkinghub.elsevier.com/retrieve/pii/S0038092X24004377.

[22] U. Egerer, S. Dana, D. Jager, B.J. Stanislawski, G. Xia, S. Yellapantula, Field measurements reveal insights into the impact of turbulent wind on loads experienced by parabolic trough solar collectors, Sol. Energy 280 (2024) 112860, http://dx.doi.org/10.1016/j.solener.2024.112860, URL: https://linkinghub.elsevier.com/retrieve/pii/S0038092X24005553.

[23] U. Egerer, S. Dana, D. Jager, G. Xia, B.J. Stanislawski, S. Yellapantula, Wind and structural loads data measured on parabolic trough solar collectors at an operational power plant, Sci. Data 11 (1) (2024) 98, http://dx.doi.org/10.1038/s41597-023-02896-4.

[24] U. Egerer, S. Dana, B. Stanislawski, D. Jager, G. Xia, S. Yellapantula, Wind and structural loads on parabolic trough solar collectors at Nevada Solar One, 2023, http://dx.doi.org/10.25984/2001061, URL: https://data.openei.org/submissions/5938. *Open Energy Data Initiative (OEDI)*.

[25] R. Hurt, W. Yim, R. Boehm, M.J. Hale, R. Gee, Advanced parabolic trough field testing: real-time data collection, archiving, and analysis for the solargenix advanced parabolic trough, in: Solar Energy, ASMEDC, Denver, Colorado, USA, 2006, pp. 49–54, http://dx.doi.org/10.1115/ISEC2006-99078, URL: https://asmedigitalcollection.asme.org/ISEC/proceedings/ISEC2006/47454/49/319135.

[26] J.M. Christian, C.K. Ho, Finite element modeling of concentrating solar collectors for evaluation of gravity loads, bending, and optical characterization, in: ASME 2010 4th International Conference on Energy Sustainability, Volume 2, ASMEDC, Phoenix, Arizona, USA, 2010, pp. 475–481, http://dx.doi.org/10.1115/ES2010-90050, URL: https://asmedigitalcollection.asme.org/ES/proceedings/ES2010/43956/475/348081.

[27] G. Zhu, A. Lewandowski, A new optical evaluation approach for parabolic trough collectors: First-principle optical intercept calculation, J. Solar Energy Eng. 134 (4) (2012) 041005, http://dx.doi.org/10.1115/1.4006963, URL: https://asmedigitalcollection.asme.org/solarenergyengineering/article/doi/10.1115/1.4006963/444620/A-New-Optical-Evaluation-Approach-for-Parabolic.

[28] A. Hachicha, I. Rodríguez, J. Castro, A. Oliva, Numerical simulation of wind flow around a parabolic trough solar collector, Appl. Energy 107 (2013) 426–437, http://dx.doi.org/10.1016/j.apenergy.2013.02.014, URL: https://linkinghub.elsevier.com/retrieve/pii/S0306261913001220.

[29] K.S. Anderson, C.W. Hansen, W.F. Holmgren, A.R. Jensen, M.A. Mikofski, A. Driesse, pvlib python: 2023 project update, J. Open Source Softw. 8 (92) (2023) 5994, http://dx.doi.org/10.21105/joss.05994.

[30] I. Reda, A. Andreas, Solar position algorithm for solar radiation applications, Sol. Energy 76 (5) (2004) 577–589, http://dx.doi.org/10.1016/j.solener.2003.12.003, URL: https://www.sciencedirect.com/science/article/pii/S0038092X0300450X.

[31] NREL's Solar Position Algorithm (SPA), 2003, https://midcdmz.nrel.gov/spa/. (Accessed 08 August 2023).

[32] K. Anderson, M. Mikofski, Slope-Aware Backtracking for Single-Axis Trackers, Technical Report NREL/TP–5K00-76626, 1660126, MainId:7307, 2020, http://dx.doi.org/10.2172/1660126, URL: https://www.osti.gov/servlets/purl/1660126/.